Chapter 5: New Insights in Turbulent Heat Transfer with Oil and Hybrid Nano-oils, Subject to Discrete Heating, for Parabolic Trough Absorbers

As discussed in the literature review, a parabolic trough absorber (PTC absorber) is subject to non-uniform heating (see figure 1.2). In this chapter, the discrete heating condition, an extreme of such a heating condition, is considered for (a) assessing the limitations and applicability of the well-known computational fluid dynamics (CFD) approaches and (b) in-depth understanding of the heat transfer and fluid process in a PTC absorber with such a special heating condition, and (c) investigating the limitations of the generalized Nusselt number correlation and developing a way for adopting the same for such an extreme heating condition. These are presented subsequently.

5.1 Computational Fluid Dynamics Framework

This section presents the performed 3D CFD analyses for the turbulent flow of pure and hybrid nano-oils through a long, straight, horizontal tube, subject to the different heat fluxes at the upper and the lower halves. This problem's selection is motivated by using standard approaches, like wall function and correlations for the surface-area-averaged Nusselt number, for simulating heat transfer in a parabolic trough absorber. The adopted detailed methodology for assessing such fundamental and applied aspects is presented subsequently.

5.1.1 Problem Description

The 3D geometry of the modeled copper tube with the boundary conditions is depicted in Figure 5.1. It is worth mentioning that an identical geometry has been installed in the laboratory for performing experiments with pure and nano-oils. Thus, the findings will be

helpful in a better understanding and assessment of the experimental findings in the long run. The total length of tube L = 4 m is equally divided into heated and unheated regions, the inner diameter of tube D_i = 0.023 m, and the outer diameter of tube D_{out} = 0.025 m. Thus, L/D_i = 86.95 is sufficient for obtaining the statistical, hydraulically fully-developed flow field in the unheated region, which serves as the inlet condition for the heated region.

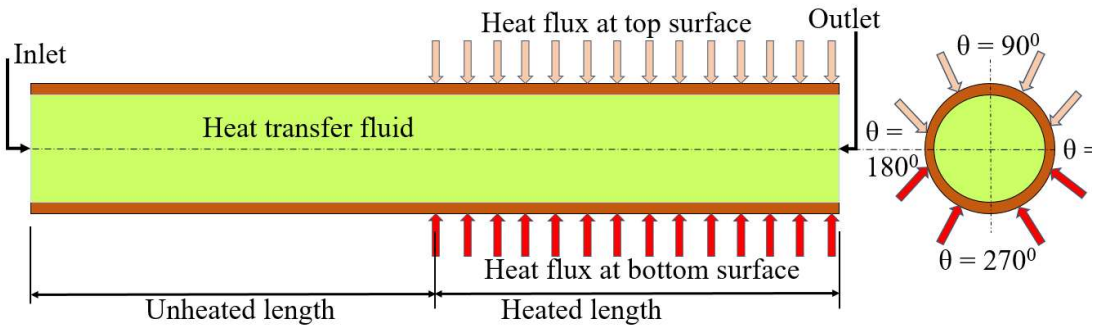

Figure 5.1 Schematic of the 3D straight, long tube with boundaries for computational fluid dynamics analyses.

The straight tube is divided into two halves, viz. the top surface for $0 < \theta \leq 180^0$ and the bottom surface for $180^0 < \theta \leq 360^0$. This arrangement allows different heat fluxes on the top and bottom surfaces. The top and bottom surfaces are subject to the same heat flux for uniform heating conditions, which are subject to different heat fluxes for discrete heating conditions. The bottom surface is maintained at 50 kW/m2 (50 Suns) for the reported simulations, and different heat fluxes are applied to the top surface. The resulting heat flux ratio q_r = 1, 5, 10, 20, 40, and 50 (Table 5.1). The simulations are performed for Reynolds number 5000 – 20000, which are relevant for a parabolic trough absorber. Therminol VP1 (TVP1) is selected as the working fluid for the CFD investigations. It is worth mentioning that the extreme heat flux ratio, q_r = 50, is motivated by the concentrated radiation *only* onto the lower half of the absorber tube, and the upper half is exposed to solar irradiance. All the other heat flux ratios are motivated by the presence of a secondary

reflector that focuses a part of the concentrated solar irradiance onto the upper half of the absorber tube. Indeed, the distribution for concentrated solar irradiance on the lower half of the parabolic trough absorber is rather continuous. Thus, using a uniform high heat flux of 50 Suns on the lower half and a lower uniform heat flux on the upper half can be considered extreme conditions. Therefore, the findings will be helpful for intermediate better scenarios.

Table 5.1 The applied heat fluxes on the top and bottom surfaces of the tube for CFD analyses.

Heat flux on the top for $0 < \theta \leq 180^0$ $(q_t^{"})$ in kW/m^2	Heat flux on the bottom for $180^0 < \theta \leq 360^0$ $(q_b^{"})$ in kW/m^2	Heat flux ratio (q_r)
50	50	1
10		5
5		10
2.5		20
1.25		40
1		50

The generated structured mesh for 3D analyses is shown in Figure 5.2. This includes the thickness of the tube for conjugate heat transfer analyses. The generated grid with $r+ = 1$ resolves the viscous boundary layer adequately for the first point near the wall. The differently structured meshes are generated for the grid independence test, discussed in sub-section 5.1.3.1.

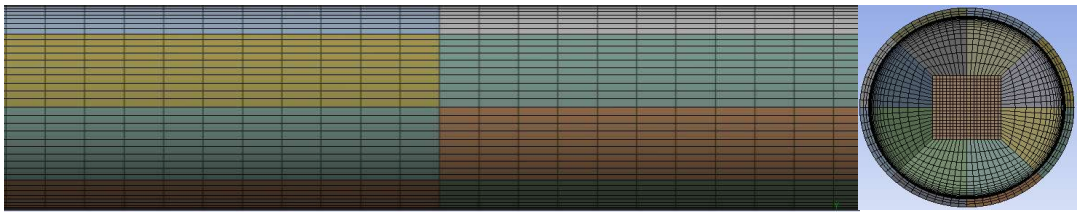

Figure 5.2 Generated structured mesh for 3D computational fluid dynamics analyses.

5.1.2 Mathematical Modeling

Researchers use a single-phase or multiphase approach to study the effect of nanoparticles in the base fluid. This chapter selects the single-phase approach, assuming that the nanoparticles and base fluid are in thermal equilibrium and the local velocity is the same for nanoparticles and base fluid [41]. The governing RANS equations, including energy, were already presented in chapter 4. Based on the reported findings and recommendations from the previous chapter, the realizable K-ε model with enhanced wall treatment is selected based on a detailed comparative assessment with standard K-ε models [34][127][128].

5.1.2.1 Boundary Condition and Numerical Scheme

The following boundary conditions are applied to solve the coupled non-linear partial differential equations: (a) uniform velocity U_{in} along the axial direction, temperature T_{in} = 373.15 K, and turbulence intensity $I = 0.16\, Re^{\left(-\frac{1}{8}\right)}$ [127], are specified at the fluid inlet (b) zero temperature gradient, P_{guage}= 0, and the turbulence intensity is specified as the fluid outlet, (c) no-slip boundary conditions are specified at the inner wall of the tube, and (d) adiabatic boundary condition for the unheated length, $0 \leq z\ (\text{in m}) < 2,$ and heat fluxes for the heated length, $2 \leq z\ (\text{in m}) \leq 4,$ are specified at the outlet wall of tube (see Table 5.1).

The Reynolds-averaged equations for continuity, momentum, energy, K, and ε are discretized using the second-order upwind scheme. The spatial discretization for the gradient is evaluated using the least square cell-based values in the simulation. The Semi-Implicit Pressure-Linked equation (SIMPLE) scheme is used to solve this for *p-v* coupling during numerical solution. In this equation, pressure correction is derived; during each iteration, pressure is updated by applying pressure correction supplied to the momentum equation so that the resulting velocity field should satisfy the continuity equation. The temperature-dependent thermophysical properties of fluids and solids are taken from the literature (see Table 5.2). The convergence criterion is set to 10^{-6} for the scaled residuals of time-averaged- velocity, temperature, K, and ε. The ANSYS 19.2 version is used for the simulations.

Table 5.2 The adopted thermophysical properties of fluids and solids for CFD analyses.

Material/oil/ nano-oil	Equations/correlations
Copper [32] [63]	$\rho = 8933$ (kg m^{-3}) $c_P = 285.8 + 0.44631T - 5.2054 \times 10^{-4}T^2 + 2.3958 \times 10^{-7}T^3$ (J kg^{-1}K^{-1}) $k = 441.6 - 0.17119T + 1.5446 \times 10^{-4}T^2 - 7.2917 \times 10^{-8}T^3$ (W m^{-1}K^{-1})
Al_2O_3 [32][63]	$\rho = 3970$ (kg m^{-3}) $c_P = -531.43 + 7.135T - 0.011923T^2 + 9.3125 \times 10^{-6}T^3 - 2.7679 \times 10^{-9}T^4$ (J kg^{-1}K^{-1}) $k = 148.14 - 0.56883T + 9.794 \times 10^{-4}T^2 - 8.0417 \times 10^{-7}T^3 + 2.5595 \times 10^{-10}T^4$ (W m^{-1}K^{-1})

TVP1[32][129]	$\rho = 1.4386 \times 10^{-3} - 1.8711T + 2.737 \times 10^{-3}T^2 - 2.3793 \times 10^{-6}T^3$ (kg m^{-3}) $c_P = 2.125 \times 10^3 - 11.017T + 0.049862 \times T^2 - 7.7663 \times 10^{-5}T^3 + 4.392 \times 10^{-8}T^4$ (J kg^{-1}K^{-1}) $k = 0.14644 - 2.0353 \times 10^{-5}T - 1.9367 \times 10^{-7}T^2 + 1.0614 \times 10^{-11}T^3$ (W m^{-1}K^{-1}) $\mu = 0.023165 - 0.1476 \times 10^{-3}T + 3.617 \times 10^{-7}T^2 - 3.9844 \times 10^{-10}T^3 + 1.6543 \times 10^{-13}T^4$ Pa.s
Nanofluid /hybrid nanofluid [32][115] [101][98]	$\rho_{hnf} = (1-\phi)\rho_{bf} + \phi_1\rho_{np1} + \phi_2\rho_{np2}$ (kg m^{-3}), where $\phi = \phi_1 + \phi_2$ $C_{phnf} = \frac{(1-\phi)\rho_{bf}C_{pbf} + \phi_1\rho_{np1}C_{pnp1} + \phi_2\rho_{np2}C_{pnp2}}{\rho_{hnf}}$ (J kg^{-1}K^{-1}) $k_{nf} = \left[(3\phi - 1)k_{np} + (2 - 3\phi)k_{bf} + \sqrt{\Delta}\right]$ (W m^{-1}K^{-1}) where $\Delta = \left[(3\phi - 1)k_{np} + (2 - 3\phi)k_{bf}\right]^2 + 8k_{np}k_{bf}$ (W^2 m^{-2}K^{-2}) $k_{hnf} = \frac{k_{nf1}\phi_1 + k_{nf2}\phi_2}{\phi}$ (W m^{-1}K^{-1}) $\mu_{hnf} = \mu_{bf}(123\phi^2 + 7.3\phi + 1)$ (Pa s)

5.1.2.2 Data Deduction

The non-dimensional velocity U^+ and the non-dimensional radial position r^+ are computed as follows:

$$U^+ = \frac{u}{u_\tau} \tag{5.1}$$

where the frictional velocity $u_\tau = \sqrt{\frac{\tau_w}{\rho}}$ and the wall shear stress $\tau_w = \mu \frac{\partial u}{\partial r}\Big|_{r=R}$ with

$$r^+ = \frac{(R-r)u_\tau}{\upsilon} \tag{5.2}$$

The local, bulk-mean, fluid temperature $T_{m,z}$, area-averaged heat transfer coefficient at the top $(h_{t,z})$ and bottom $(h_{b,z})$ surfaces are computed using the following equation 5.3-5.6:

$$T_{m,z} = \frac{\int \rho c_p u T dA}{\int \rho c_p u dA} \tag{5.3}$$

$$T_{m,z} = \frac{\int \rho c_p u T dA}{\int \rho c_p u dA} \tag{5.4}$$

$$h_{t,z} = \frac{q_t^{"} \times D_{out}}{D_i \times (T_{wt,z} - T_{m,z})} \tag{5.5}$$

$$h_{b,z} = \frac{q_b^{"} \times D_{out}}{D_i \times (T_{wb,z} - T_{m,z})} \tag{5.6}$$

where $T_{wt,z}$, $T_{wb,z}$, and $T_{wo,z}$ are surface-area-averaged wall temperatures for the top and bottom surfaces, and surface-area-averaged wall temperatures, respectively, at an axial location. Also, the local, surface-area-averaged Nusselt number for the top $(Nu_{t,z})$ and bottom $(Nu_{b,z})$ surfaces, and the overall Nusselt number $(Nu_{o,z})$ are computed using the following equation 5.7 -5.9.

$$Nu_{t,z} = \frac{h_{t,z} \times D_i}{k_z} \tag{5.7}$$

$$Nu_{b,z} = \frac{h_{b,z} \times D_i}{k_z} \tag{5.8}$$

$$Nu_{o,z} = \frac{q_o^{"} \times D_{out}}{k_z (T_{wo,z} - T_{m,z})} \tag{5.9}$$

where $q_o^{"}$ is the overall heat flux, which is the average of heat fluxes at the top and bottom surfaces. The above expressions are obtained using the conservation of energy principle and Newton's law of cooling. Finally, the obtained values from equations 5.7-5.9 are integrated over the entire length to calculate the $\overline{Nu}_t, \overline{Nu}_b, \overline{Nu}_o$. Finally, to deduce separate Nusselt number correlations for top and bottom surfaces, $\overline{Nu}_{corr(b)or(t)}$, the following power law is assumed:

$$\overline{Nu}_{corr(b)or(t)} = C_1 {Nu_{gen}}^{l} {q_r}^{m} \quad (5.10)$$

In equation 5.10, Nu_{gen} defines the deduced generalized Nusselt number correlation for nanofluids/hybrid nanofluid deduced in chapters 3 and 4. Such an approach will enable the adaptation of an existing correlation for such heating conditions.

5.1.3 Grid Independence Test and Validation

5.1.3.1 Grid Independence Test

Three structured meshes of different resolutions are generated for the grid independence test. These are coarse with 0.75 million nodes, medium with 1.6 million nodes, and fine with 3.2 million nodes. A uniform heat flux of 50 kW/m^2 is applied on the outer surface of the tube for this investigation. The simulations are performed for *Re* = 20000. The axially varying, time-averaged fluid temperature at the centerline and the inner wall temperature, for $2 \leq z$ (in m) < 4 are selected (see Figure 5.3). It is evident from Figure 5.3a that (a) the heat is transferred to the centerline for $z > 2.25$ m, and (b) the inner wall temperature sharply rises to about 424 K until $z = 2.1$ m and then gradually attains the maximum value of about 434 K at $z = 4$ m. These are attributed to the non-linear heat transfer coefficient along the flow direction in the heated section. The comparative assessment in Figure 5.3 reveals that the numerical solution is practically independent of the mesh sizes. Thus, the medium mesh with 1.6 million nodes is used for the subsequent analyses.

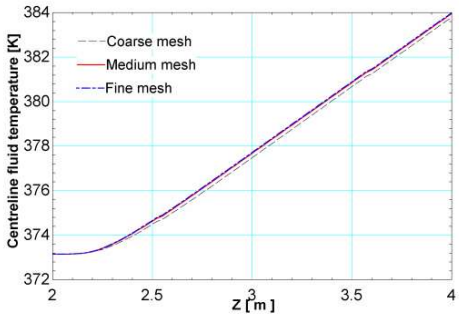

a)

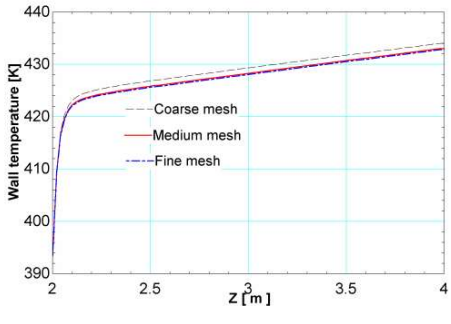

b)

Figure 5.3 Grid independence test using the time-average, axially varying a) fluid temperature at the centreline and b) the inner wall temperature for $2 \leq z\ (\text{in m}) < 4$.

5.1.3.2 Validation

RANS simulations are performed to validate the numerical framework for *Re* = 20000. As a first step, the computed time-averaged, non-dimensional axial velocity is compared (U^+) with the well-known logarithmic law in the turbulent boundary layer. This can be approximated using the following, region-wise, descriptions near the wall:

$$\text{Viscous sub-layer: } U^+ = r^+ \; 0 < r^+ < 5 \tag{5.11}$$

$$\text{Logarithmic law region: } U^+ = A \ln r^+ + B \text{ for } 35 \leq r^+ \leq 350 \tag{5.12}$$

where A = 2.5 and B = 5.5 [130][131].

Figure 5.4a illustrates the CFD-based U^+, which is obtained using the coarse, medium, and fine grids at an axial position *z* = 1.9 m for *Re* = 20000. The following can be observed:

a. The computed U^+ values represent the viscous sub-layer region reasonably well for $0 < r^+ < 5$.
b. The computed U^+ values resemble the logarithmic law region for $60 < r^+ < 500$, and the deviation from the logarithmic law is evident in the outer region. The logarithmic law is extended to a lower *r*+ value only for identifying the buffer region, which should not be interpreted otherwise.
c. The computed values for U^+ are practically comparable for all the selected meshes. This means the numerical framework applies to hydraulic simulation.

Subsequently, a comparison between the RANS-based surface-area-averaged Nusselt number with the Gnielinski correlation-based values is presented in Figure 5.4b for TVP1 with $5000 \leq Re \leq 20000$ and $q_r = 1$. It is evident from this assessment that the numerical framework provides an acceptable prediction for the overall surface-area-

averaged values for the Nusselt number. The above observations confirm that the adopted numerical framework is applicable for further computations and that the medium mesh is indeed sufficient.

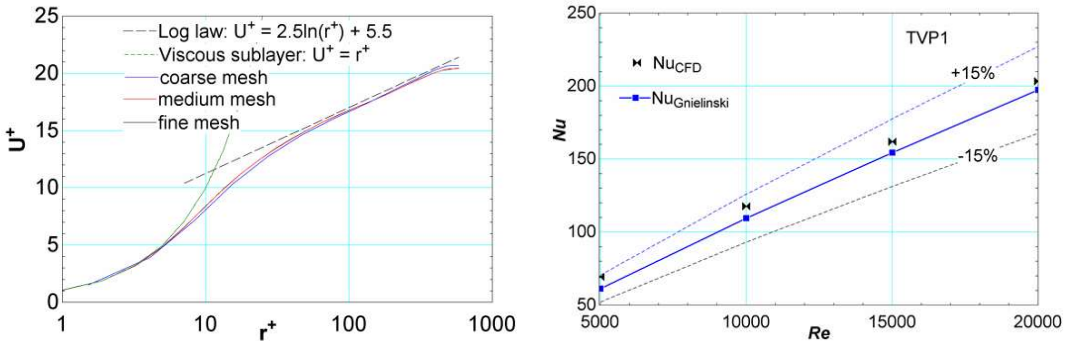

Figure 5.4 Comparison between (a) CFD analyzed and wall-law for U^+ with coarse, medium, and fine meshes at z = 1.9 m and Re = 20000, and (b) CFD analyzed overall, surface-area-averaged, Nusselt number (Nu_{CFD}) and the Gnielinski correlation ($Nu_{Gnielinski}$) for TVP1 with $5000 \leq Re \leq 20000$ and $q_r = 1$.

5.2 Results and Discussion

This section uses the presented numerical framework to report the findings from RANS computations for the turbulent flow of pure and hybrid nano-oils, with discrete heating. These simulations are performed by suppressing the body force due to gravity by specifying $g = 0$ m/s^2 and activating the body force by specifying $g = 9.81$ m/s^2. The objectives are (a) to understand the effect of gravity on simulating the flow and heat transfer, (b) to assess the capabilities and limitations of the usually adopted modeling assumptions, and (c) to analyze the top, bottom, and overall Nusselt number for the special heating conditions. The findings are presented subsequently:

5.2.1 Axial Velocity Contour

The axial velocity contours are presented in Figure 5.5 at the different axial (z) locations in the heated section for TVP1 with Re = 5000 and q_r = 1, 50. Here, the location z = 2.0 m indicates the inlet to the heated section, where the axial velocity follows the time-averaged, fully-developed, turbulent flow profile for gravity-suppressed and gravity-included RANS simulations. Interestingly, a low-speed flow region is observed near the upper wall at a later axial location, say z > 2.1 m, including the gravity effect for q_r = 1 and 50. Because of the mass balance, a higher axial velocity is observed near the lower wall for these conditions. This allows inferring a growing flow asymmetry along the axial direction for the time-averaged axial velocity. The axial velocity contour does not reveal such flow asymmetry for the RANS simulations without gravity. This allows concluding that the inclusion of gravity is necessary, even for a horizontal tube, to simulate the turbulent heat transfer.

Axial Location (z)	q_r = 1, Re = 5000, g = 0 m/s^2	q_r = 1, Re = 5000, g = 9.81 m/s^2	q_r = 50, Re = 5000, g = 0 m/s^2	q_r = 50, Re = 5000, g = 9.81 m/s^2
	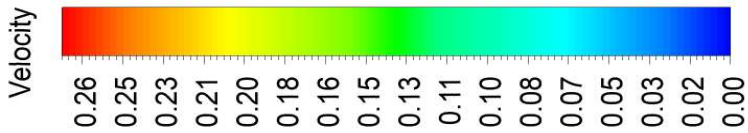			
2 m	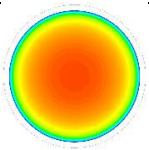	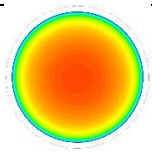	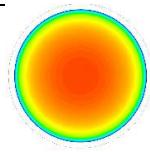	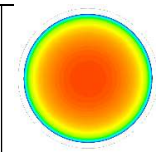
2.05m	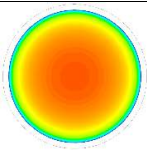	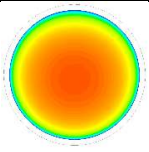	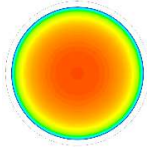	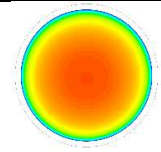

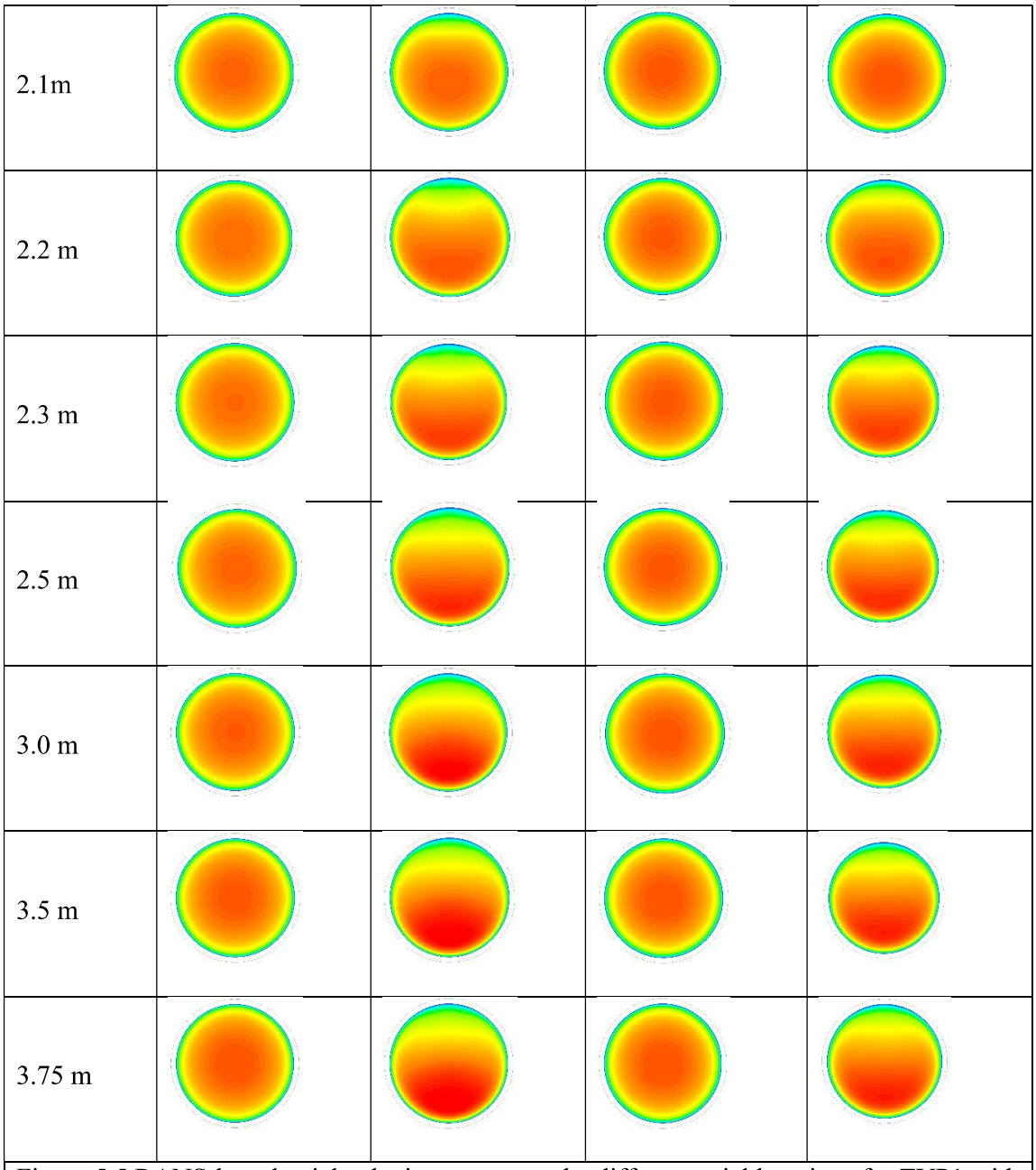

Figure 5.5 RANS-based axial velocity contour at the different axial locations for TVP1 with Re = 5000, without and with gravity effect (g = 0 and 9.81 m/s^2), and different heat flux ratios (q_r = 1 and 50).

Figure 5.6 shows the RANS-analyzed axial velocity contours at the different axial locations, in the heated section, for TVP1 with Re = 20000 and q_r = 1, 50. These do not reveal any asymmetry, as for Re = 5000, including the gravity effect. Moreover,

qualitatively, the contours seem unchanged for $2.00 \leq z(m) \leq 3.75$. Therefore, it can be concluded that the effect of gravity is insignificant for the turbulent flow at a very high Reynolds number. However, for the sake of completeness, the inclusion of buoyancy or gravity is recommended for simulating the turbulent heat transfer in the parabolic trough absorber with azimuthally varying heat flux. So far, a qualitative analysis has been presented for the axial velocity for the discrete heating condition. As a next step, a quantitative analysis is presented to understand the observed time-averaged flow features better.

Axial Location (z)	q_r = 1, Re = 20000, g = 0 m/s^2	q_r = 1, Re = 20000, g = 9.81 m/s^2	q_r = 50, Re = 20000, g = 0 m/s^2	q_r = 50, Re = 20000, g = 9.81 m/s^2
	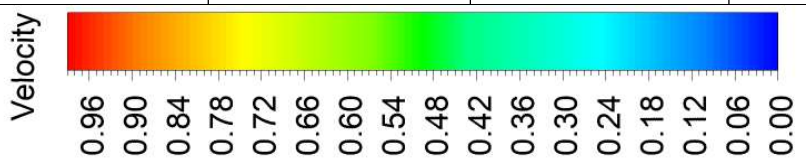			
2.00 m	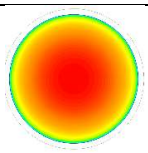	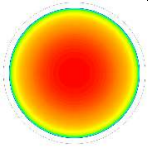	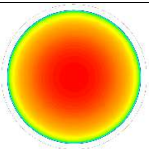	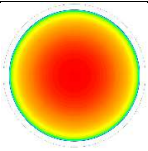
2.3 m	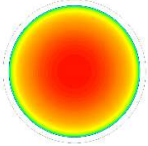	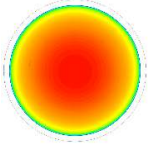	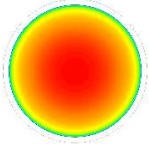	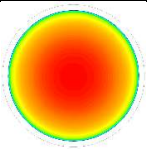
3.0 m	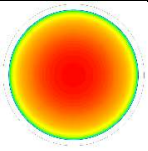	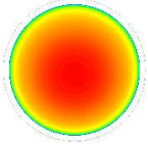	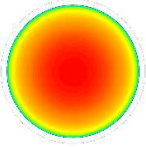	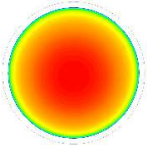

3.75 m	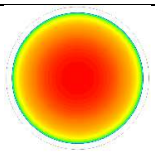	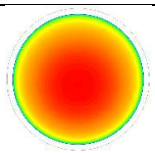	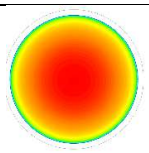	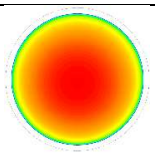

Figure 5.6 RANS-based axial velocity contour at the different axial locations for TVP1 with Re = 20000, without and with gravity effect (g = 0 and 9.81 m/s^2), and different heat flux ratios (q_r = 1 and 50).

5.2.2 Radial Distribution of the Axial Velocity

Radial distributions for the time-averaged axial velocity for TVP1 are depicted at several axial locations, $2.0 \leq z(m) \leq 3.75$, in Figure 5.7. In this figure, r = 0 indicates the centreline, r < 0 indicates the lower half, and r > 0 indicates the upper half along the diagonal line connecting θ = 90 º and 270 º (see Figure 5.2). The length-to-diameter ratio for pipe in the unheated length is about 86.9. This is sufficient for achieving the hydraulically fully-developed flow at the inlet to the heated section at z = 2.0 m. The following may be observed from the assessment of Figure 5.7:

i. For simulations without gravity, the time-averaged axial velocity distribution, along the axial direction for $2.0 \leq z(m) \leq 3.75$, remains practically symmetric about the centreline at r = 0, for Re = 5000 and 20000. At the same time, the effect of gravity in the simulations leads to asymmetry around the centreline at r = 0 for the axial velocity profile.

ii. For simulations including the effect of gravity, a higher time-averaged axial velocity, for $2.0 \leq z(m) \leq 3.75$, is observed in the lower half (r < 0) in comparison to the upper half (r > 0) in the heated region at Re = 5000. This reveals the convective acceleration of the fluid near the lower wall and convective deceleration near the upper wall. However, for Re = 20000, the effect of gravity seems to be

suppressed, and the usual, symmetric, turbulent velocity profile is obtained. Thus, deviation from the standard logarithmic law is expected in the heated tube for the simulations, including the effect of gravity at Re = 5000. This will be assessed subsequently.

iii. The maximum value for time-averaged axial velocity increases for $r < 0$ and decreases for $r > 0$ along the axial direction at Re = 5000. The increasing and decreasing values for the statistical axial velocity along the axial direction are indicated by dotted upward/downward arrows. For q_r = 1, the maximum, time-averaged, axial velocity is $0.25 < U_{max} < 0.276$ for $2.0 \leq z(m) \leq 3.75$ at Re = 5000. For q_r = 50, the values for the maximum, time-averaged, axial velocity are $0.25 < U_{max} < 0.265$ for $2.0 \leq z(m) \leq 3.75$ at Re = 5000. Interestingly, the maximum value for time-averaged axial velocity is marginally lower for q_r = 50 than q_r = 1. Accordingly, the convective deceleration near the upper wall may be higher for q_r = 50 than q_r = 1. The calculated mass flow rate through the upper half and lower half of the tube cross-section, for q_r = 1 and at Re = 5000, are provided in Table 5.3 for a closer inspection. It is evident that the mass flow rate, though the tube cross-section's lower half, is greater than that of the upper half of the tube cross-section. Also, the mass flow rate through the lower half increases along the axial direction, whereas the same decreases for the upper half of the tube for a given total mass flow rate of 0.0863 *kg/s*.

Table 5.3 Mass flow rate through the upper and lower half of the cross-section, at various axial locations, including the effect of gravity, and for q_r = 1, at Re = 5000.

Axial location (z)	The mass flow rate through the upper half ($\dot{m}_t$ kg/s)	The mass flow rate through the lower half ($\dot{m}_b$ kg/s)	Total mass flow rate $\dot{m_{total}} = \dot{m}_t + \dot{m}_b$ (kg/s)
2 m	0.0429	0.0434	0.0863
2.05 m	0.0423	0.0440	
2.3 m	0.0387	0.0476	
3.0 m	0.0380	0.0483	
3.75m	0.0379	0.0484	

iv. The presence of high-speed flow near the lower wall and low-speed flow near the upper wall will affect the heat transfer coefficient. Therefore, different values for the Nusselt number are expected at the lower and upper walls.

Without gravity effect (g = 0) With gravity effect (g = 9.81 m/s^2)

q_r=1

Re = 5000

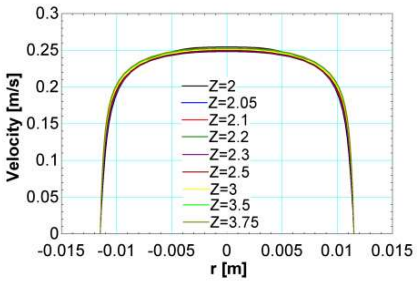

a)

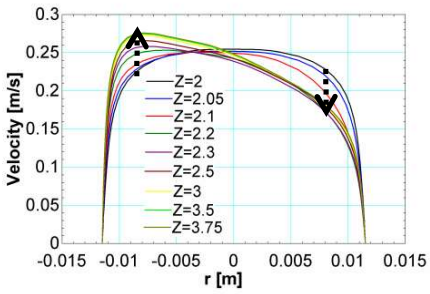

b)

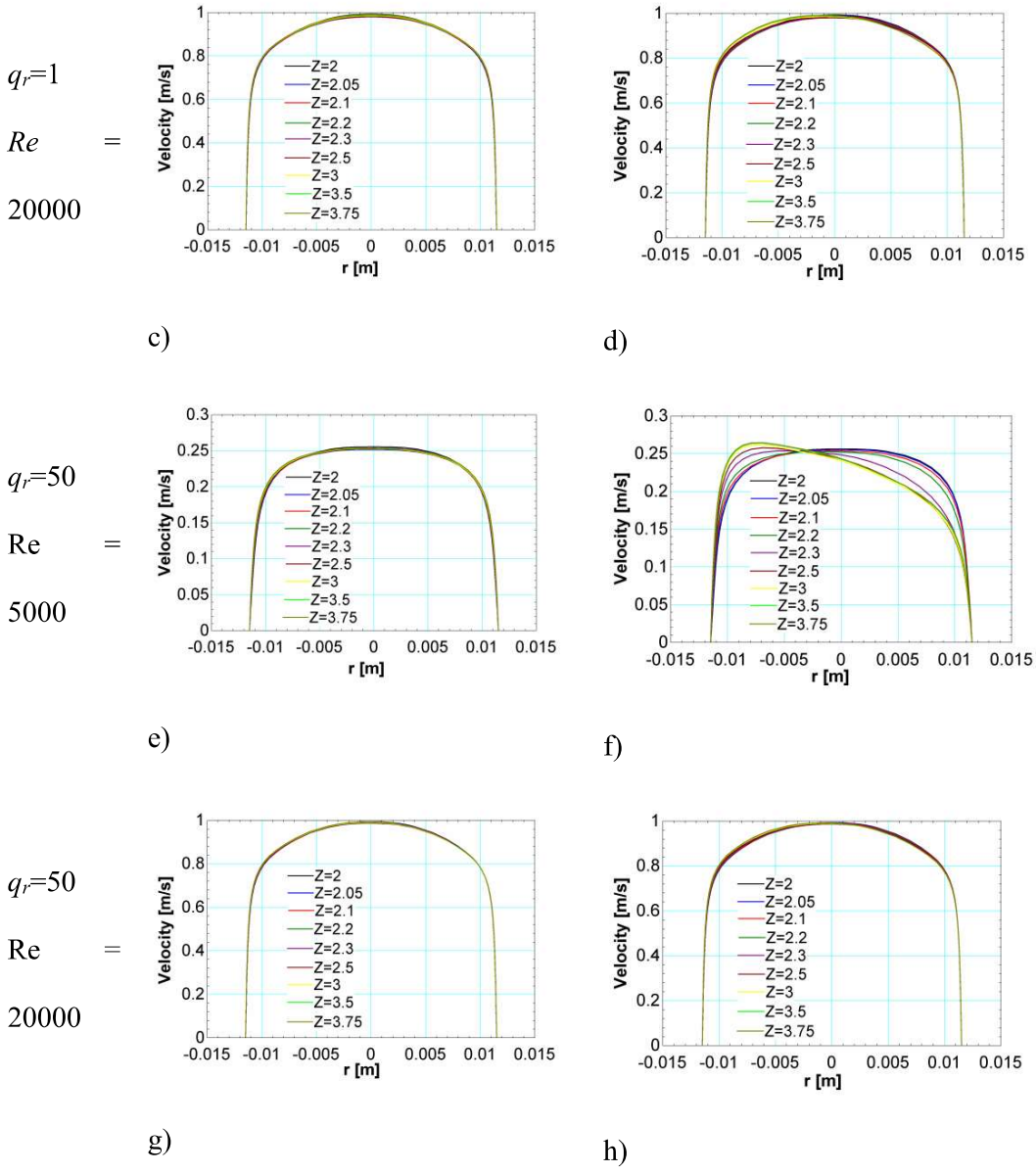

Figure 5.7 RANS-based axial velocity for simulations without gravity effect and with gravity effect, different Reynolds number *Re* = 5000 and 20000, and different heat flux ratios q_r=*1* and 50.

A comparison between the RANS-based non-dimensional, statistical, axial-velocity U^+ and the standard wall law is performed, with and without the effect of gravity (Figure 5.8), at $\theta = 90^0$ and 270^0 with *Re* = 5000, and different heat flux ratios q_r = 1 and 50 at z = 3.75. The following can be inferred from the investigation of Figure 5.8:

a. The computed U^+ values for simulation without the effect of gravity (with g = 0 m/s^2) at θ = 90^0 and 270^0 are the same, and their deviations from the standard logarithmic law are evident. The presence of a log-linear region is not obvious.

b. The computed U^+ values for simulations with the effect of gravity (with g = 9.81 m/s^2) revealed a wide variation concerning the logarithmic law. The higher values for U^+ at $\theta = 90^0$ compared to the described logarithmic law are attributed to the relatively lower values for the frictional velocity-based turbulent wall shear stress and, therefore, the convective deceleration. The calculated values for the same are summarized in Table 5.4.

c. The computed lower values for U^+ (with g = 9.81 m/s^2), concerning the logarithmic law, at $\theta = 270^0$, is attributed to the higher values for the turbulent wall shear stress on this wall (see Table 5.4). Interestingly, for the simulations without the effect of gravity (g = 0 m/s^2), the turbulent wall shear stress values are independent of the azimuthal location. This observation concludes that gravity induces secondary flow, which is investigated using streamlines.

d. Further analyses of U^+ revealed the presence of a log-linear region for $30 < r^+ < 305$ at $\theta = 90^0$ and for $40 < r^+ < 85$ at $\theta = 270^0$, and q_r = 1, 50. This means the standard logarithmic law should be adapted. This concludes the need for a generalized logarithmic law, depending on the thermophysical properties of a fluid, which can be applied to a wide range of heat flux ratios for the parabolic trough absorber. In other words, using standard logarithmic law for simulating turbulent heat transfer in a parabolic trough absorber is inappropriate. *One question arises: is there any non-dimensional parameter that can be used to assess coefficients A and B in equation 5.12*?

The abovementioned observations explain some of the reported observations, especially using logarithmic law for simulating a parabolic trough absorber with circumferentially varying heat flux.

Table 5.4 The RANS-analyzed wall shear stress (τ in Pa)

Heat flux ratio (q_r)	τ (in Pa) with g = 9.81m/s^2	τ (in Pa) with g = 0
1 (at θ = 90^0)	0.07	0.14
1 (at θ = 270^0)	0.24	0.14
50 (at θ = 90^0)	0.10	0.17
50 (at θ = 270^0)	0.25	0.17

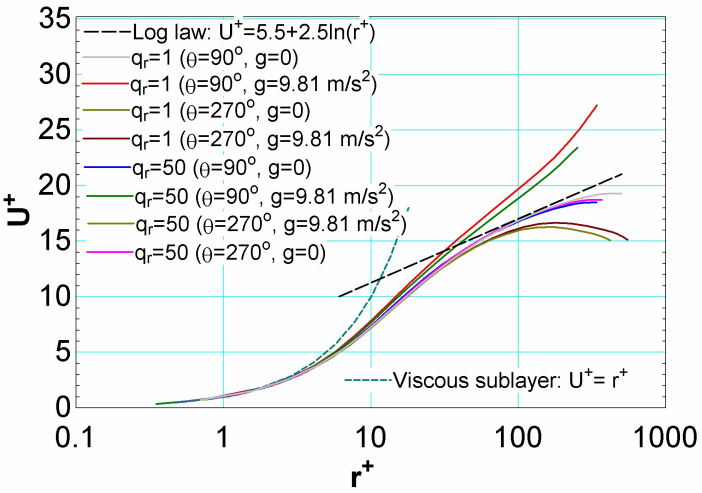

Figure 5.8 A comparison between the RANS-analyzed non-dimensional axial velocity with the standard logarithmic law at θ = 90^0 and θ = 270^0 for simulations without and with the effect of gravity.

5.2.3 Streamline

The above discussion reveals for simulations including the effect of gravity and Re = 5000 (a) the asymmetry in time-averaged axial velocity, (b) a higher fluid velocity for $r < 0$ in comparison to $r > 0$ along the diagonal line connecting $\theta = 90$ º and 270 º, and (c) deviation of the time-averaged, statistical, U^+ from the corresponding logarithmic law. As expected, the presence of secondary flow is depicted using the streamlines, at the different axial locations, in Figure 5.9. These show the presence of counter-rotating vortices on the depicted axial planes for the heat flux ratios q_r = 1 and 50. For q_r = 1, the symmetrically located vortices are observed, whereas for q_r = 50, the asymmetry is quite evident, say at z = 3.0 m. Interestingly, the distortions in the streamlines are observed for q_r = 1, marked with a circle, which is not the case for q_r = 50. Unfortunately, an explanation for this observation is unavailable now; however, the need for unsteady simulations is realized. This is out of this paper's scope and will be performed in the future. It may be noted that no such relevant secondary flows are observed for Re = 20000; thus, the same is not discussed. Further investigations are performed to evaluate the effect of gravity on heat transfer. These are presented subsequently.

Axial Location (z)	q_r = 1, Re = 5000, g = 9.81 m/s^2	q_r = 50, Re = 5000, g = 9.81 m/s^2
2.0 m	 a)	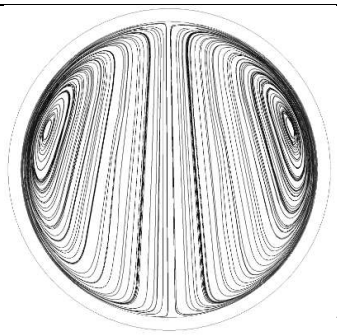 b)

2.5 m	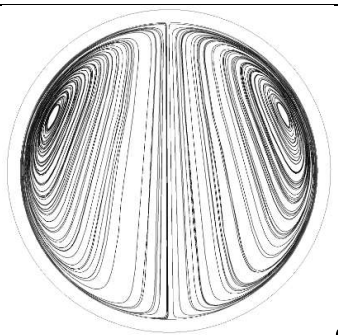 c)	 d)
3.0 m	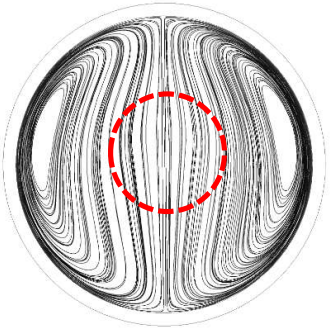 e)	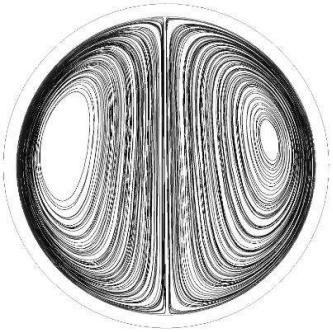 f)
3.75 m	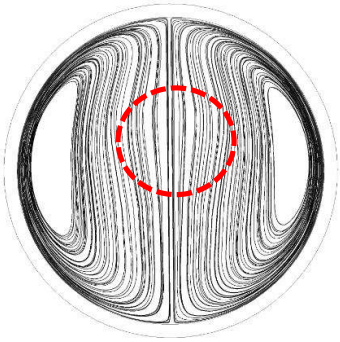 g)	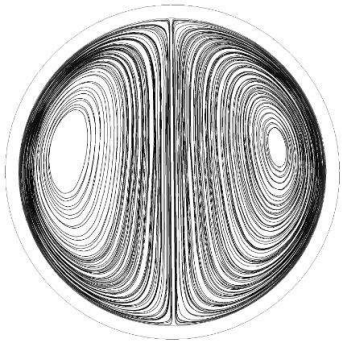 h)

Figure 5.9 The RANS-analyzed streamlines at various axial locations for q_r = 1 and q_r = 50, considering the effect of gravity at *Re* = 5000.

5.2.4 Temperature Contour

In line with the previous observations, the RANS-based time-averaged temperature contours are shown in Figure 5.10 for $2.0 \leq z(m) \leq 3.75$ with *Re* = 5000, q_r = 1, 50, and g = 0, 9.81 m/s^2. The selected axial locations are the same as the axial velocity contours in Figure 5.7. The following can be inferred from these temperature contours at the different axial positions:

a. The presence of a high-temperature region around θ = 90 º is observed for simulations, including the effect of gravity for q_r = 1 and 50. The dotted circle/elliptical shapes identify these. This is attributed to the effect of gravity, which promotes the movement of warmer fluid from the lower wall region ($r < 0$) to the upper wall region ($r > 0$). Consequently, the radial temperature distribution is expected to be asymmetric around the centreline, which is investigated subsequently. The computations ignoring the effect of gravity do not reveal any such phenomenon and remain practically symmetric around the centreline.

b. The high-temperature region near the upper wall is wider for q_r = 1 compared to q_r = 50 for g = 9.81 m/s^2. This counter-intuitive observation is attributed to the combined effect of applied high heat flux on the upper wall for q_r = 1 compared to q_r = 50, and a lower speed of TVP1 for Re = 5000 near the upper wall in comparison to the lower wall (see Figure 5.7).

c. The solid (copper) temperature is independent of the azimuthal position for the simulations with q_r = 1 and g = 0 m/s^2. This is expected, considering the applied uniform heat flux on the periphery and the same speed of TVP1 near the upper and lower walls (see Figure 5.7). This is, thus, consistent with the previous point assessment and emphasizes a proper understanding of the fluid flow-related heat transfer for the parabolic trough absorber.

d. Contrary to the findings for simulations with g = 0 m/s^2, a higher solid temperature is obtained at the upper wall for the simulations with g = 9.81 m/s^2 in the heated section for q_r = 1. This vital observation allows concluding the possible failure of the parabolic trough absorber near the upper half. This condition needs particular attention, considering the recent inclusion of a secondary reflector with a parabolic

trough absorber to enhance the flux concentration on the upper half, thereby reducing the heat flux ratios.

e. The computed solid temperature at the lower wall for q_r = 50 is higher with g = 0 m/s^2 compared to g = 9.81 m/s^2. This is attributed to the higher speed of TVP1 near the lower wall in comparison to the upper wall. However, generally, the lower wall temperature is higher than the upper wall, and thus, failure of the lower wall is expected in such a case. This is important for the parabolic trough absorber without any secondary reflector in which the lower half of the tube is exposed to the concentrated solar irradiance (say 50 Suns) and the upper half is exposed to the direct normal irradiance (say 1 Sun).

Axial Location (z)	q_r = 1, Re = 5000, g = 0 m/s^2	q_r = 1, Re = 5000, g = 9.81 m/s^2	q_r = 50, Re = 5000, g = 0 m/s^2	q_r = 50, Re = 5000, g = 9.81 m/s^2
	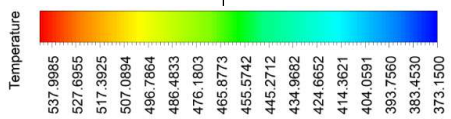		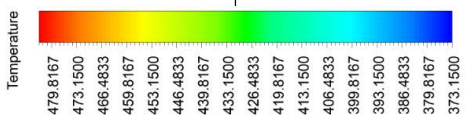	
2 m	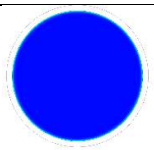	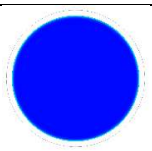	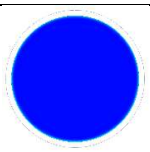	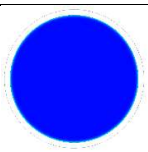
2.05 m	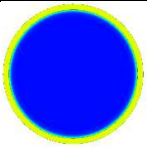	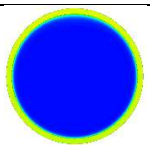	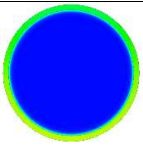	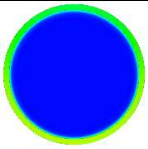
2.1 m	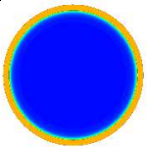	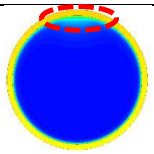	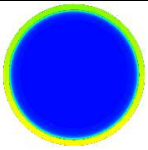	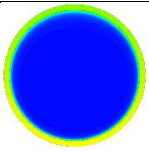

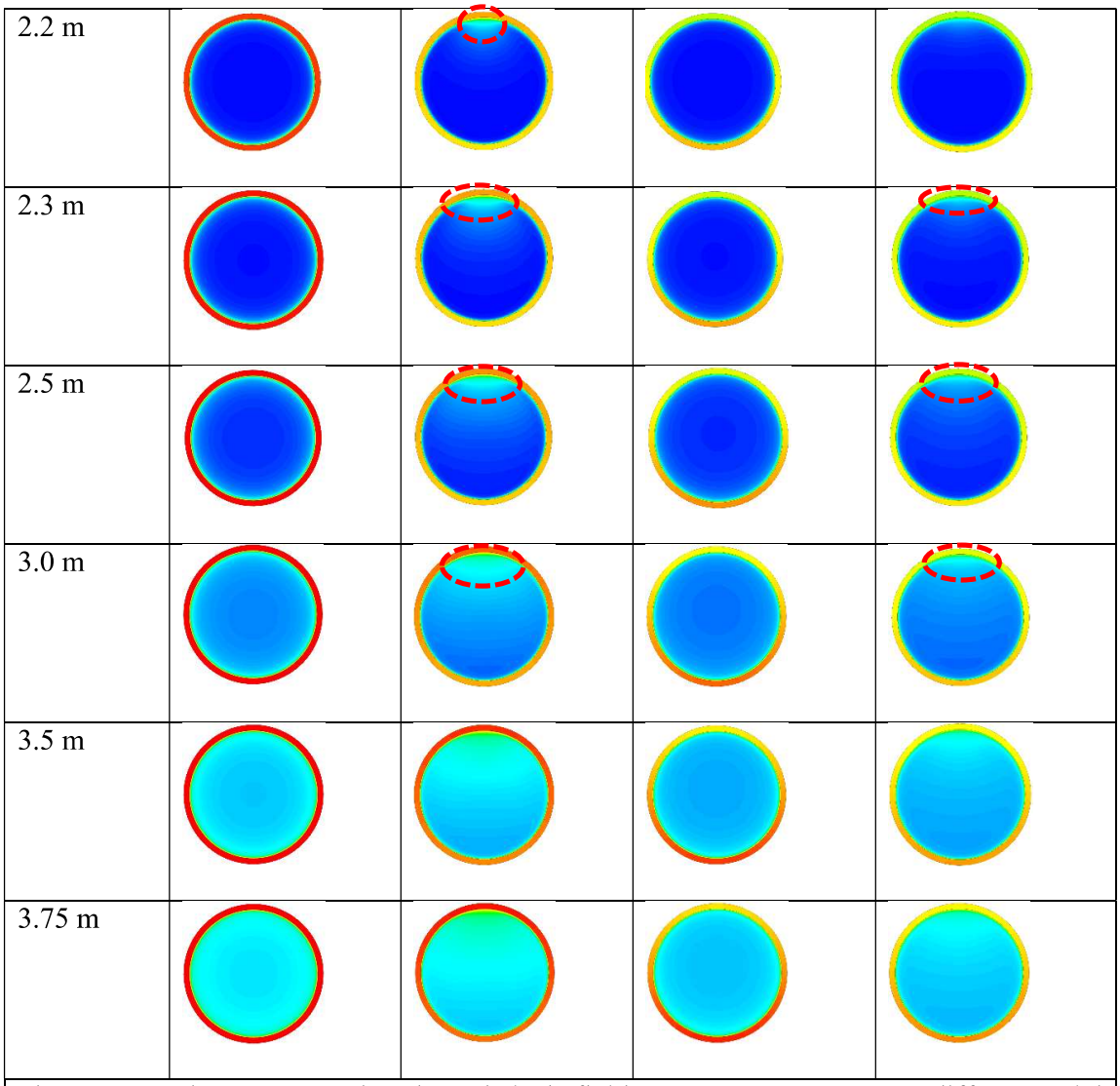

Figure 5.10 The RANS-analyzed, statistical, fluid temperature contour at different axial locations for Re = 5000, g = 0, 9.81 m/s^2, and different heat flux ratios q_r = 1 and 50.

A similar qualitative assessment of the statistical temperature contour in Figure 5.11 for Re = 20000 with and without gravity leads to obvious results. Such as the peripheral symmetry of solid temperature for q_r = 1, the lower wall temperature is higher than that of the upper wall for q_r = 50, and the fluid temperature seems comparable for g = 0 and 9.81 m/s^2 at the different axial locations with q_r = 1, and fluid temperature is higher at a radial position $r < 0$ than that of $r > 0$ for q_r = 50 and g = 0, 9.81 m/s^2. In other words, the effect

of gravity for simulations at a high *Re* is insignificant. A detailed quantitative assessment for the radial distribution of the time-averaged fluid temperature is performed subsequently to analyze the related heat transfer.

Axial Location (z)	q_r = 1, Re = 20000, g = 0 m/s^2	q_r = 1, Re = 20000, g = 9.81 m/s^2	q_r = 50, Re = 20000, g = 0 m/s^2	q_r = 50, Re = 20000, g = 9.81 m/s^2
	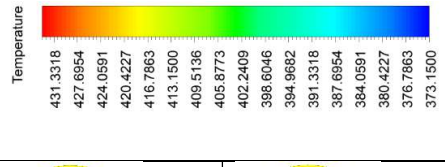		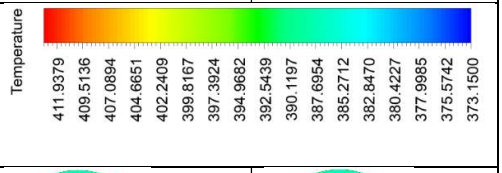	
2.05 m	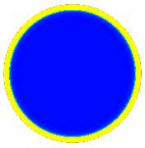	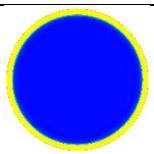	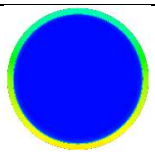	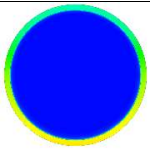
2.3 m	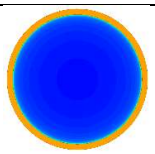	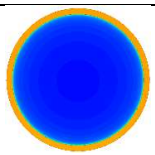	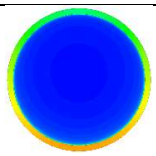	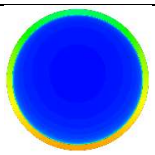
3.0 m	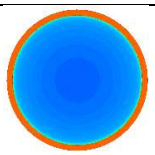	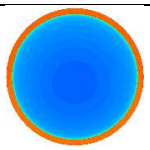	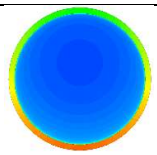	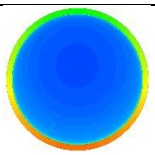
3.75 m	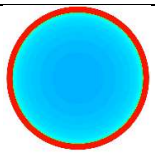	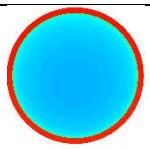	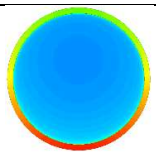	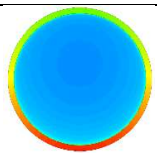

Figure 5.11 The RANS-analyzed, statistical, fluid temperature contour at different axial locations for *Re* = 5000, g = 0, 9.81 m/s^2, and different heat flux ratios q_r = 1 and 50.

5.2.5 Radial Distribution of Statistical Temperature for TVP1

The radial distributions of statistical temperature for TVP1 are used for the quantitative investigation with Re = 5000, 20000, q_r = 1, 50, and g = 0, 9.81 m/s^2 (see Figure 5.12). These are shown at different axial locations, $0 \leq z(m) \leq 3.75$, along the diagonal line connecting θ = 90 º and 270 º, as for the axial velocity (see Figure 5.7). Thus, an effort is made to corroborate the findings from fluid flow and heat transfer analyses. The temperature distribution over the small thickness of the copper tube is evident for all the cases and, therefore, is not discussed further. The following can be inferred for the fluid temperature from Figure 5.12:

a. The fluid temperature distribution is symmetric around r = 0 for q_r = 1, g = 0 m/s^2, and Re = 5000, 20000. This is expected as gravity-induced anisotropy or asymmetry is absent. The resulting highest fluid temperature near the upper and lower wall is about 550 K for Re = 5000 and 430 K for Re = 20000. This can be attributed to a higher heat transfer coefficient for Re = 20000 than Re = 5000. A detailed assessment of the computed Nusselt number is presented subsequently.

b. The asymmetry of fluid temperature around r = 0 is observed for q_r = 1, g = 9.81 m/s^2, and Re = 5000. The fluid temperature is higher near the upper wall than the lower wall for q_r = 1, g = 9.81 m/s^2, and Re = 5000. This is consistent with the lower flow speed near the upper wall compared to the lower wall. At the same time, no such asymmetry is observed for Re = 20000, which is consistent with the computed statistical axial velocity (see Figure 5.7).

c. A comparison of the fluid temperature for Re = 5000 reveals (i) a self-similar profile for $z \geq$ 3.0 m with g = 0 and 9.81 m/s^2, (ii) a higher bulk mean temperature for g = 9.81 m/s^2 in comparison to g = 0 m/s^2, which leads to a reduction in wall temperature by about 15-25K, and (c) a marginally higher temperature near the upper wall for g

= 9.81 m/s^2, which is already explained using the temperature contour. In other words, the gravity effect mitigates the risk of failure of a parabolic trough absorber tube by redistributing the fluid or reducing the solid temperature.

d. For the simulation with q_r = 50 and Re = 5000, the lower wall temperature (at r < 0) is about 480 K for g = 0 m/s^2 and about 470 K for g = 9.81 m/s^2. This allows the conclusion that gravity enhances the heat transfer from the lower wall. Thus, different heat transfer coefficients or Nusselt numbers are expected at the lower and upper walls. Moreover, the Nusselt number will be a function of the azimuthal position. A detailed analysis of the same is provided subsequently.

e. For the simulation with q_r = 50 and Re = 20000, the fluid temperatures are practically the same near the upper and lower wall for g = 0 and 9.81 m/s^2. This is consistent with the findings that the effect of gravity is insignificant for such a high Re.

f. For the simulations with gravity at Re = 5000, the computed statistical fluid and solid temperatures are provided for q_r = 5, 10, 20, 40, and 50 in Figure 5.13a. This figure shows that on decreasing the heat flux ratio from 50 to 5, statistical fluid and solid temperature increases due to total heat input; also, there is an asymmetry due to discrete heating. The temperature profile at various radial locations for q_r = 10, 20, and 40 lies between q_r = 5 and 50.

From the above investigations, it may be safely concluded that the effect of gravity plays a significant role in the risk or failure assessment for parabolic trough absorbers. Also, for a high Re, an artificial inclination of the absorber concerning the horizontal surface may induce the effect of gravity, which will be beneficial for its long-term operation. This aspect may be investigated in the future. Further investigations revealed a similar trend for the

hybrid nano-oils. Thus, the same is not presented. However, an in-depth analysis of their influence on the Nusselt number is shown in the next section.

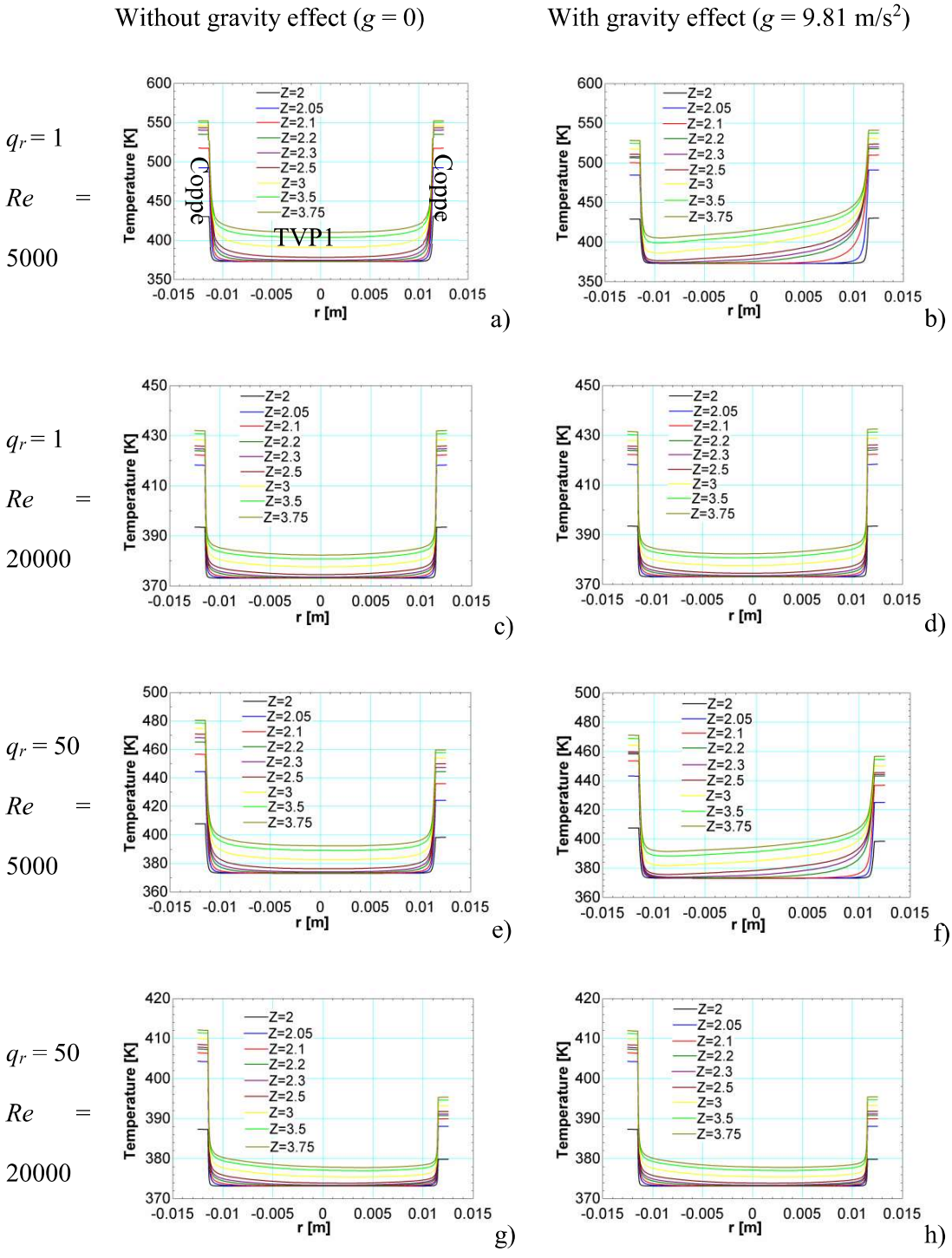

Figure 5.12 *(a - h)* RANS-based statistic fluid and solid temperatures for simulations without gravity effect and with gravity effect, different Reynolds number Re = 5000 and 20000, and different heat flux ratios q_r = 1 and 50.

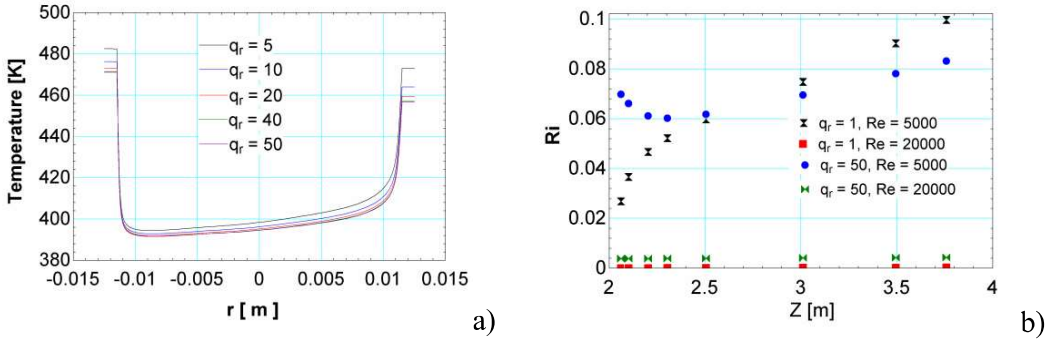

a) b)

Figure 5.13 RANS-based (a) fluid and solid temperature for q_r = 5, 10, 20, 40, and 50 simulations with gravity effect at z = 3.75 m, Re = 5000, and q_r = 5, 10, 20, 40, and 50. (b) Richardson number using the maximum temperature difference, local thermophysical properties for TVP1, and Re = 5000 and 20000 along the axial direction.

It is evident from the above discussion that the temperature difference between the upper and lower walls, including the effect of gravity, plays an important role in heat transfer. *Therefore, one obvious question arises: is the heat transfer regime, viz. natural, mixed, and forced convection, the same for both Re = 5000 and 20000?* This has a consequence on the local heat transfer. Therefore, to understand this aspect, the local Richardson number ($Ri = Gr/Re^2$) is computed for TVP1 using the maximum temperature difference and temperature-dependent thermophysical properties of the fluid at several axial locations (see Figure 5.13b). Indeed, for Re = 20000, the calculated $Ri << 0.1$, and thus, the forced convection regime is concluded. However, for Re = 5000, $0.02 \leq Ri \leq 0.1$ for $2 \leq z(m) \leq 4$, and therefore the forced-to-mixed convection regime is expected for both q_r = 1 and 50. Interestingly, the trend for Ri is the opposite, with q_r = 1 and 50 up to 2.5 m. This can be attributed to the combined effect of applied different heat fluxes and the

developing thermal boundary layer (see Figure 5.12). Subsequently, the increasing nature of *Ri* with the axial positions is consistent with the applied heat flux. This investigation also leaves a clue that *Ri* may be used to approximate the coefficients (*A* and *B*) in the wall law for *U*+ for such different conditions. Furthermore, it is noteworthy that for $Ri << 0.1$, these coefficients provide an acceptable prediction for *U* +. Further investigation on this topic is envisaged for the future.

5.2.6 Surface-Area-Averaged Nusselt Number for Oil and Hybrid Nano-Oils

So far, RANS-analyzed flow and temperature fields are used to describe the effect of gravity, heat flux ratio, and Reynolds number (a) on the modeling approaches, e.g., the use of wall-function may be case specific, (b) on the occurrence of high- and low- speed fluid flow region near the lower and upper wall, respectively, (c) on the presence of low- and high- temperature regions near the lower and upper wall, respectively, and (d) on the different heat transfer regimes along the flow direction. *The final question arises: how do these phenomena affect the Nusselt number on the long, straight tube with discrete heating*? This aspect is investigated here using TVP1 and Cu-Al_2O_3-TVP1 with different V/V% ($\emptyset$) of nanoparticles.

The RANS-analyzed, surface-area-averaged, Nusselt numbers for TVP1 and Cu-Al2O3-TVP1 with $1 \leq \emptyset\ (\frac{V}{V}\%) \leq 6$, $5000 \leq Re \leq 20000$, $1 \leq q_r \leq 50$, and $g = 9.81$ m/s^2 are presented in Figure 5.14. The simulations excluding the effect of gravity are not considered for obvious reasons. This figure includes the overall surface-area-averaged Nusselt number ($\overline{Nu_0}$), the surface-area-averaged Nusselt number on the top surface ($\overline{Nu_t}$), and surface-area-averaged Nusselt number on the bottom surface ($\overline{Nu_b}$). The following can be inferred from this figure:

a. The values for $\overline{Nu_0}$ using TVP1 and Cu-Al_2O_3-TVP1 with $\emptyset = 1\,\frac{V}{V}\%$ are practically independent of the heat flux ratios (Figures 5.14a and 5.14c). The same is checked for validation using TVP1 in sub-section 5.1.3.2. In reality, the values for Nu_t at $0 < \theta \leq 180^0$ are much smaller than $\overline{Nu_b}$ at $180^0 < \theta \leq 360^0$ with $4 \leq \frac{\overline{Nu_b}}{\overline{Nu_t}} \leq 12$ for TVP1 and Cu-Al_2O_3-TVP. This is consistent with the steeper fluid temperature near the bottom surface ($r < 0$) in comparison to the top surface ($r > 0$), which can easily be inferred from Figure 5.12. Therefore, using the overall surface-area-averaged Nusselt number is inappropriate for assessing the maximum thermal stress on a parabolic trough absorber, which is exposed to different heat fluxes at the top and bottom surfaces. Thus, the need for a corrected Nusselt number is realized for the top and bottom surfaces.

b. The RANS-based values for $\overline{Nu_t}$ its decreasing trend at the top surface and $\overline{Nu_b}$ revealed its increasing trend at the bottom surface, indicated by vertically upward and downward arrows, for $5 \leq q_r \leq 50$ and a given *Re*. Moreover, it may be observed that the differences between the values of $\overline{Nu_b}$ for $5 \leq q_r \leq 50$ increase with *Re*. This may be attributed to the relative decreasing effect of gravity on the heat transfer with the increasing *Re*. This re-affirms an observation that gravity enhances the mixing or mitigates the risk of failure for parabolic trough absorber at a low *Re*.

c. Figure 5.14b shows the effect of volume fraction for nanoparticles, $1 \leq \emptyset\ (\frac{V}{V}\%) \leq 6$, on $\overline{Nu_0}$, $\overline{Nu_t}$, and $\overline{Nu_b}$. This figure reveals that Nu_0 increases up to 11% for *Re* = 20000, which is expected. It is interesting to note that a rather negligible change in the values for $\overline{Nu_t}$ with $\emptyset$ and a noteworthy change for $\overline{Nu_b}$ with $\emptyset$.

d. Figure 5.14c shows that the reported, generalized Nusselt number correlation for the turbulent flow of hybrid nanofluids (Nu_{gen}) developed in chapter 4, predicts

the overall surface-area-averaged values with Cu-Al_2O_3-TVP1 for $\emptyset = 1\ \frac{v}{v}\%$ within the reported uncertainty of about ± 15 %. In other words, this correlation can be adapted for the surface-area-averaged values at the top and bottom surfaces with a correction factor based on the heat flux ratios.

e. Realizing the beneficial effect of gravity for mitigating thermal stress-related failure by enhancing the Nusselt number, the installation of a parabolic trough absorber at a small tilt angle is recommended. This is necessary to assess the risk of failure arising out of the thermal gradient in the solid for a parabolic trough absorber, which is exposed to different heat fluxes on the top (upper half) and bottom (lower half) surfaces. An attempt is made to address this vital aspect, and Nusselt number correlations for the upper and lower surfaces are deduced, $\overline{Nu}_{corr(b)\ or\ (t)}$ as a function of heat flux ratios and Nu_{gen} shown in equation 5.10. The unknown coefficients (*l* and *m*) are estimated using the regression analysis from the computed data for Cu-Al_2O_3-TVP1 at *Re* = 5000 and 20000, and $1 \leq q_r \leq 50$. It is worth noting that only a part of the computed data is used for this purpose, and the deduced correlations are as follows:

$$Nu_{corr(b)} = 3.757 {Nu_{gen}}^{0.743} {q_r}^{0.115} \quad (5.13)$$

$$Nu_{corr(t)} = 1.192 {Nu_{gen}}^{0.981} {q_r}^{-0.786} \quad (5.14)$$

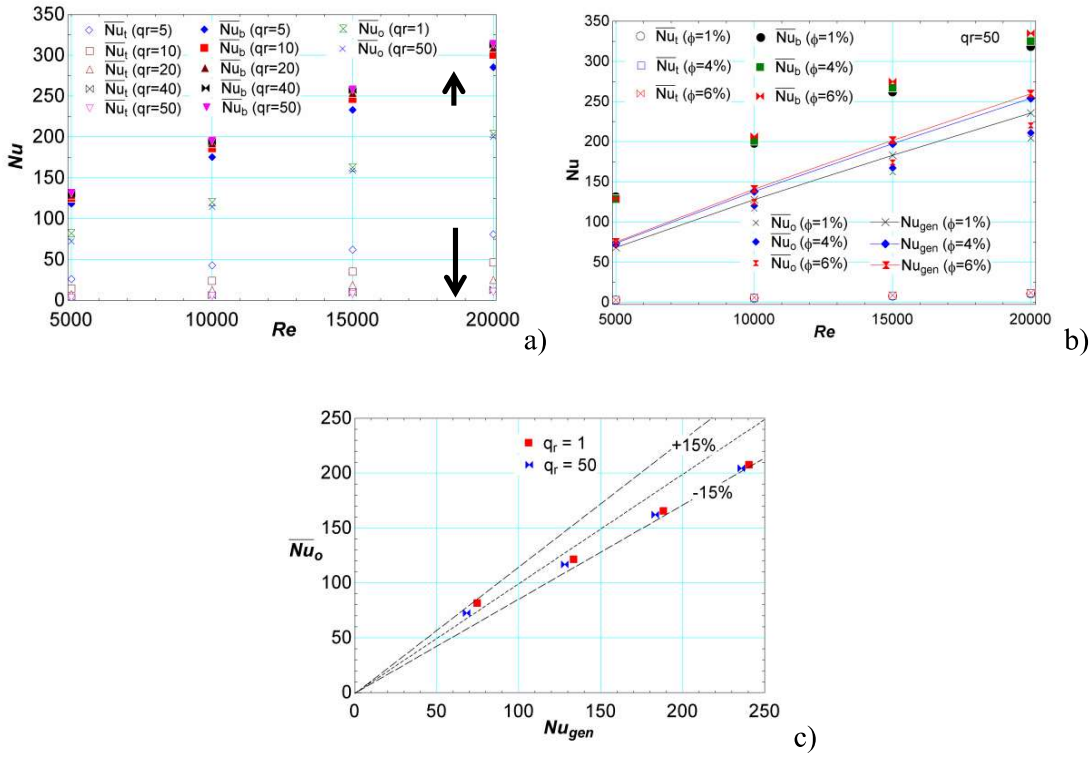

Figure 5.14 The RANS-based surface-area-averaged Nusselt number (a) for pure TVP1, (b) for Cu-Al_2O_3-TVP1, $1 \leq \emptyset\ (\frac{V}{V}\%) \leq 6$, and (c) is compared with Nu_{gen} for Cu-Al_2O_3-TVP1 with $\emptyset\ = 1\ \frac{V}{V}\%$, q_r = 1 and 50. For these simulations, $5000 \leq Re \leq 20000$ and $1 \leq q_r \leq 50$ are selected.

As a next step, the deduced Nusselt number correlations are tested using the remaining data for *Re* =10000 and 15000 within an uncertainty of about ±15% (shown in figure 5.15). It is worth noting that these correlations adopt an existing, validated, generalized correlation for hybrid nanofluids.

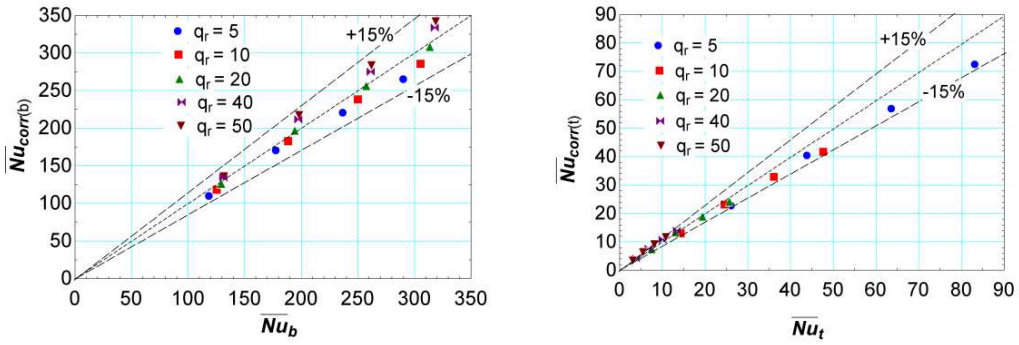

a) b)

Figure 5.15 Comparison of (a) $\overline{Nu_b}$ (b) $\overline{Nu_t}$ *with* $\overline{Nu_{corr}}$ for Cu-Al_2O_3-TVP1 with $\emptyset = 1 \frac{V}{V}\%$, and for simulations $5000 \leq Re \leq 20000$ and $5 \leq q_r \leq 50$ are selected.

5.3 Summary

The chapter deals with the Reynolds-averaged Navier Stokes (RANS)-based analyses for turbulent heat transfer in a long straight tube subjected to discrete heating conditions. This problem's selection is motivated by the different values of average heat flux on the lower and upper surfaces for a parabolic trough absorber in various industrial processes like drying, bleaching, processing heating, distillation, separation, and pulp preparation. The simulations are performed considering the reported literature for Reynolds number $5000 \leq Re \leq 20000$, heat flux ratios between the bottom and top surfaces $1 \leq q_r \leq 50$, without or with buoyancy or gravity effect by numerically prescribing g = 0 or 9.81 m/s^2. The simulations are performed for pure Therminol VP1 (TVP1) and Cu-Al_2O_3-TVP1 (hybrid nano-oils) with the different volume fractions of nanoparticles $\left(1 \leq \emptyset \ (\frac{V}{V}\%) \leq 6\right)$. The validation exercise revealed that the Gnielinski correlation predicts the overall surface-area-averaged Nusselt number with TVP1 within ±10%. Moreover, the reported generalized correlation for hybrid nanofluids predicts the overall surface-area-averaged

Nusselt number with Cu-Al_2O_3-TVP1 within the reported uncertainty ±15%. Following are the notable findings and recommendations arising out of this paper:

i. The effect of gravity gets suppressed with the increasing *Re*. For *Re* = 5000, gravity enhances the local fluid flow speed near the bottom surface and reduces the local fluid flow speed near the top surface. For Re = 5000, q_r = 1, the maximum relative increase in the axial velocity of about 8.5%, concerning the fully developed centreline velocity at the inlet, is obtained at the non-dimensional radial position $\frac{r}{r_0} \sim 0.69$, near the lower wall, where the radius of the tube r_0 = 0.0115 m. At the symmetrically located radial position, the relative decrease in the axial velocity near the upper wall is about 28%.

ii. The standard logarithmic law is inadequate for the non-dimensional, time-averaged, axial velocity *U*+ for such problems. Thus, a grid resolution of about *y*+ = 1 is recommended for simulating the turbulent heat transfer problem in a parabolic trough absorber. Further analyses leave a clue that the coefficients in the standard logarithmic law may be corrected with the Richardson number (*Ri*).

iii. The surface-area-averaged Nusselt number for the bottom surface ($180^0 < \theta \leq 360^0$) is much higher than that of the top surface ($0^0 < \theta \leq 180^0$). The ratio between these two Nusselt number is 4 to 12. Thus, using an overall, surface-area-averaged Nusselt number is inadequate to assess the risk of failure for a parabolic trough absorber. Consequently, the need to include a correction factor in the Gnielinski and generalized correlations is realized to estimate the surface-area-averaged values on the top and bottom surfaces.

iv. Using the expression of the computed value for the Nusselt number for top and bottom surface-area-averaged values is deduced. These are as follows:

$$Nu_{corr(t)} = 1.192 {Nu_{gen}}^{0.981} {q_r}^{-0.786}$$

$$Nu_{corr(b)} = 3.757 {Nu_{gen}}^{0.743} {q_r}^{0.115}$$

Finally, it may be concluded that gravity promotes the redistribution of thermal energy at an axial plane. In other words, exploiting the effect of gravity will help mitigate the risk of thermal stress-related failure. Therefore, the horizontal installation of a parabolic trough absorber is not recommended, and the use of a small tilt angle, even for oils, should be preferred.